U-series disequilibria generated by partial melting of spinel lherzolite

Dirk Landwehr [1], Jon Blundy *, Eva Maria Chamorro-Perez [2], Eddy Hill, Bernard Wood

CETSEI, Department of Earth Sciences, University of Bristol, Wills Memorial Building, Bristol BS8 1RJ, UK

Abstract

We have experimentally investigated the effects of crystal chemistry on the partitioning of U and Th between clinopyroxene and anhydrous silicate melt in a wide range of synthetic systems from 1 to 8 GPa and 1330 to 1735°C. We have also generated limited additional data for garnet–melt and pigeonite–melt U–Th partitioning. We find that for sub-calcic clinopyroxenes, of the variety which characterise the mantle solidus, D_U is greater than D_{Th}, as previously predicted from theoretical considerations based on the size of the M2 site into which substitution occurs. Melt composition appears to have a minor effect on partitioning. The new partitioning data have been combined with existing experimental data to derive a thermodynamically based expression that predicts D_{Th} and D_U from crystal chemistry, pressure and temperature. This model has been combined with published experimental determinations of clinopyroxene composition along the mantle solidus to derive the variation in D_{Th} and D_U/D_{Th} during mantle melting. A simple, one-dimensional model dynamic mantle melting using the new data shows that ^{230}Th excesses, expressed as the activity ratio (^{230}Th/^{238}U), of up to 1.34 can be generated within the spinel lherzolite stability field. This value is in excellent agreement with the maximum ^{230}Th excess (1.35) observed in mid-ocean ridge basalt (MORB). The magnitude of excess correlates linearly with the depth to the onset of melting. These findings, which are relatively insensitive to plausible variations in mantle porosity and melt productivity, are consistent with observed global variations in MORB ^{230}Th excesses with ridge axial depth. We conclude that significant ^{230}Th excess can be generated by melting of spinel lherzolite, in the absence of garnet. © 2001 Published by Elsevier Science B.V.

Keywords: U-238/Th-230; clinopyroxene; partitioning; mantle; melting; spinel lherzolite; mid-ocean ridge basalts

* Corresponding author. Tel.: +44-117-9545447; Fax: +44-117-9253385; E-mail: jon.blundy@bristol.ac.uk

[1] Present address: Technische Universität Berlin, Fachgebiet Petrologie, EB 15, Strasse des 17. Juni 135, D-10623 Berlin, Germany.

[2] Present address: Laboratoire de Sciences de la Terre, UMR 5570, Ecole Normale Supérieure de Lyon, 46 Allée d'Italie, F-69364 Lyon, France.

1. Introduction

The ^{238}U-decay series is a potentially powerful tool for deciphering the nature and timescales of magmatic processes [1–4]. The parent isotope ^{238}U decays to ^{206}Pb via a decay series which includes the intermediate short-lived isotope ^{230}Th with a half-life of 75.38 ka. Mantle-derived young volcanic rocks (e.g. mid-ocean ridge basalts (MORBs) and ocean island basalts younger than approximately 350 ka) commonly display secular disequilibrium in the ^{238}U-decay series, with excesses of (^{230}Th) over (^{238}U) most frequently observed[3]. This means that ^{230}Th is preferentially fractionated into the melt phase relative to ^{238}U during mantle melting (i.e. U is more compatible in the solid residue than Th) and that melt transport is rapid relative to the half-life of ^{230}Th. These observations require the presence of a solid phase on the mantle solidus for which the ratio of partition coefficients (D) for U and Th (i.e. D_U/D_{Th}) is greater than unity, and a bulk solid partition coefficient for U, D_U^{Bulk}, of the same order as the threshold porosity at which melt is extracted [5]. Although not well-known, the latter is likely to be greater than 10^{-5} [6]. Available experimental studies for olivine, orthopyroxene and clinopyroxene, the three major mantle minerals, confirm that olivine and orthopyroxene have $D_U/D_{Th} > 1$, but very low absolute D_U values of about 10^{-5} [7], while almost all available clinopyroxene data suggest $D_U/D_{Th} < 1$ at absolute D_U of 10^{-2}–10^{-3} [7–10]. When these data are used to calculate bulk partition coefficients relevant to mantle melting the value for clinopyroxene dominates. Therefore, in the absence of an additional phase with high D_U values and $D_U/D_{Th} > 1$, excesses of ^{230}Th cannot be generated during melting in the spinel lherzolite stability field. In contrast the pyrope-rich garnets typical of mantle peridotite yield high D_U/D_{Th} values of about 4 and absolute D_U values similar to those of clinopyroxene [4,11,12]. For this reason the generation of U-decay series disequilibrium during mantle

melting is almost universally attributed to the initiation of melting in the garnet lherzolite stability field, rather than occurring entirely in the spinel lherzolite stability field.

A major shortcoming of most of the available experimental clinopyroxene partitioning data used in modelling U-decay series equilibria is that there are apparent discrepancies between experimental and natural conditions and compositions. These include both temperature and pressure and, of particular importance for the partitioning of highly charged ions, the crystal composition. For example Lundstrom et al. [10] have demonstrated that the clinopyroxene–silicate melt D_{Th} is a strong function of the concentration of Al in tetrahedral coordination in clinopyroxene. Experimental studies on the melting behaviour of lherzolite in natural and synthetic systems [13–18] show that the composition of clinopyroxene on the lherzolite solidus is extremely sensitive to changes in pressure and temperature. With increasing pressure and temperature on the lherzolite solidus, clinopyroxenes become progressively enriched in the enstatite (En), jadeite (Jd) and calcium-tschermaks (CaTs) components and depleted in the diopside (Di) component. In the simple Na_2O–CaO–MgO–Al_2O_3–SiO_2 (NCMAS) system, this corresponds to a change in clinopyroxene composition from 0.03 Na, 0.7 Ca, 1.0 Mg and 0.3 Al atoms per formula unit (apfu) at 1.2 GPa/1295°C to 0.08 Na, 0.4 Ca, 1.3 Mg and 0.4 Al apfu at 3 GPa/1531°C along the spinel lherzolite solidus (or expressed in endmember molecules from $Jd_3CaTs_{14}En_{31}Di_{52}$ at 1.2 GPa/1295°C to $Jd_8CaTs_{17}En_{54}Di_{21}$ at 3 GPa/1531°C) [15]. Most of the U–Th partitioning data from previous studies, however, refer to low pressure diopsidic clinopyroxenes (i.e. > 0.8 Ca, < 1.0 Mg and < 0.2 Al apfu or $> Di_{55}$ and $< En_{20}$) and do not take into account the different clinopyroxene composition on the mantle solidus nor its changing behaviour with increasing pressure and temperature. This is particularly unfortunate since U–Th partitioning has been shown to be strongly dependent on clinopyroxene composition [10,19].

Recently, Wood et al. [19] presented a theoretical model for the partitioning of U and Th between clinopyroxene and silicate melts, using the

---

'lattice strain' model for element partitioning of Blundy and Wood [21]. Based on the long established observation that mineral–melt partition coefficients for a series of isovalent trace elements show a near-parabolic dependence on cation radius (e.g. [22]), Blundy and Wood [21] demonstrated that trace element partitioning on a given lattice site is a function of the site radius (r_0), its Youngs's modulus (E) and the theoretical strain free partition coefficient D_0 for an element with 'ideal' radius r_0:

$$D_i = D_0 \exp\left[\frac{-4\pi E N_A}{RT}\left[\frac{r_0}{2}(r_i - r_0)^2 + \frac{1}{3}(r_i - r_0)^3\right]\right]$$

(1)

where r_i is the radius of an element i of interest, N_A is Avogadro's number, R is the gas constant and T is temperature in K. Wood and Blundy [23] applied this model to published experimental data for rare earth element (REE) clinopyroxene–melt partitioning. They found that the apparent value of r_0 for the M2 site is a simple function of clinopyroxene composition:

$$r_0^{M2} = 0.974 + 0.067 X_{Ca}^{M2} - 0.051 X_{Al}^{M1} \text{ (Å)}$$

(2)

where X_{Ca}^{M2} and X_{Al}^{M1} refer to the atomic fractions of Ca and Al on the clinopyroxene M2 and M1 sites, respectively. For the Young's modulus of the M2 site Wood and Blundy [23] extracted values by fitting Eq. 1 to experimental data and suggested dependencies on pressure and temperature derived from measurements of the elastic properties of Di:

$$E_{M2}^{3+} = 318.6 + 6.9P - 0.036T \text{ (GPa)} = 3/4 E_{M2}^{4+}$$

(3)

where P is in GPa and T in K. Using this relationship and the compositions of near-solidus clinopyroxenes in peridotite from a number of studies [13–15,17,19,20] Wood et al. [19] showed that r_0^{M2} decreases substantially with increasing pressure on the mantle solidus. Assuming that: (1) U^{4+} is the dominant species under f_{O2} conditions relevant to mantle melting; (2) Th^{4+} ($r = 1.05$ Å in 8-fold coordination [25]) and U^{4+} ($r = 1.00$ Å in 8-fold co-

ordination [25]) exclusively enter the large distorted M2 site usually occupied by Ca ($r = 1.12$ Å in 8-fold coordination [25]); and (3) the Young's modulus E of the M2 site is approximately linearly dependent on the charge of the substituent cation [21], Wood et al. [19] applied Eq. 1 to the partitioning of Th^{4+} and U^{4+} between clinopyroxene and melt. The exact description in terms of the lattice strain model is:

$$D_U / D_{Th} =$$

$$\exp\left[\frac{-4\pi E_{M2}^{4+} N_A}{RT}\left[\frac{r_0^{M2}}{2}(r_{Th}^2 - r_U^2) - \frac{1}{3}(r_{Th}^3 - r_U^3)\right]\right]$$

(4)

Substituting Eqs. 2 and 3 into Eq. 4 Wood et al. [19] were able to predict how D_U / D_{Th} should vary for clinopyroxene on the mantle solidus. They concluded that, since $r_U < r_{Th}$ and since r_0^{M2} decreases with increasing pressure, the ratio D_U / D_{Th} should increase with increasing pressure on the mantle solidus.

Fig. 1 shows the predicted variation of the D_U / D_{Th} ratio calculated from Eq. 3 plotted as a function of r_0^{M2}. The solid and broken lines are upper and lower limits, respectively, for predicted D_U / D_{Th} values calculated from ionic radii for U and Th from Shannon [25] (solid line), and revised ionic radii for U and Th of Wood et al. [19] corrected for differences in bond lengths between halides and oxides (broken line). Also plotted are new experimental D_U / D_{Th} values from Wood et al. [19] and Salters and Longhi [26] for low-Ca clinopyroxenes that closely match the compositions of clinopyroxenes on the mantle solidus and, for comparison, the experimental data for high-Ca, diopsidic clinopyroxene from previous studies [7–10,27]. Only data from experiments carried out at least one logf_{O2} unit below FMQ or run dry in graphite capsules at high pressures have been plotted to ensure that partition coefficients refer predominantly to U^{4+} (for details see [19]). The r_0^{M2} radii of experimentally produced clinopyroxenes were calculated from Eq. 2 using the reported bulk compositions. The shaded area depicts the predicted decrease in M2 site radii for clinopyroxenes on the mantle solidus from about
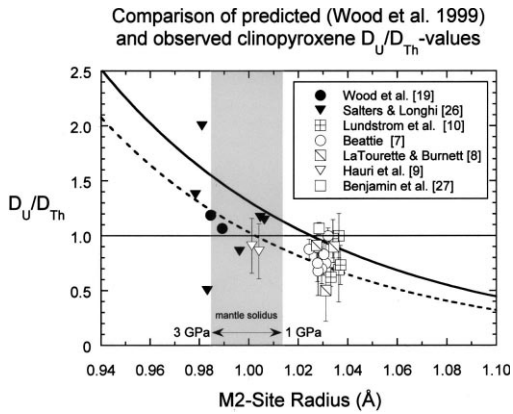
Fig. 1. Predicted (lines; Wood et al. model [19]) and observed (symbols; literature) D_U/D_{Th} values for clinopyroxene–liquid partitioning under f_{O2} conditions relevant to mantle melting. Pressure range of experiments is one atmosphere to 2.8 GPa. Solid and dashed lines refer to uncertainty in ionic radii and M2 site radius and hence give upper and lower limits of predicted D_U/D_{Th} values. Error bars (shown if bigger than symbols) are ±1 S.D. Note the scatter in the data reported by Salters and Longhi [26] for low-Ca clinopyroxene with D_U/D_{Th} ranging from 0.5 to 2.0 for the same clinopyroxene bulk compositions. No error bars are plotted for data of Salters and Longhi (see text for discussion).

can be generated by clinopyroxene without the need for garnet in the residuum. However, since the available U–Th partitioning data for low-Ca clinopyroxene stable on the mantle solidus at conditions relevant to mantle melting are few and the data reported by Salters and Longhi [26] are ambiguous because they lack an estimate of relative uncertainty (see Fig. 1) the suggestion that ^{230}Th excess can be generated by clinopyroxene alone has been received sceptically (e.g. [28]). The aim of this study was therefore to test the model predictions of Wood et al. [19] by performing U–Th partitioning experiments for a broad range of clinopyroxene compositions. In this contribution, we shall demonstrate that low-Ca clinopyroxene indeed has D_U/D_{Th} values > 1 and can potentially account for the generation of significant ^{230}Th excess within the spinel lherzolite stability field without garnet needed as a residual phase.

2. Experimental materials and methods

All experiments presented in this study were performed in the system NCMAS because a large body of experimental work reporting equilibrium clinopyroxene and silicate melt compositions already exists, and NCMAS offers a close approximation to natural systems (e.g. NCMAS makes up ∼93% of proposed upper-mantle compositions). The absence of iron from our experiments has only limited consequences for the applicability of the results to natural systems. As Mg^{2+} and Fe^{2+} mix near-ideally in most crystals and melts, partition coefficients likely scale linearly with Mg

1.013 Å at 1 GPa to 0.985 Å at 3 GPa [19]. The striking features of Fig. 1 are that, within limits of error: (1) the majority of the data plot on the trend predicted for D_U/D_{Th} by Wood et al. [19]; (2) data for high-Ca diopsidic clinopyroxene are suggestive of $D_U/D_{Th} < 1$; and (3) the limited data available for (high pressure) low-Ca clinopyroxene clearly suggest that $D_U/D_{Th} > 1$. In the context of U-series disequilibrium, these findings suggest that at pressures above 1 GPa ^{230}Th excesses

Table 1
Nominal major element compositions of starting materials

	$Di_{80}Ab_{20}$	$Di_{20}Ab_{80}$	S&H[a] AD-Na	S&H AD	W&P[b] 122-1	W&P 2311-07	W&P 2701-07	W&P P7	W&P P10
	wt%								
SiO_2	58.6	66.5	50.6	48.9	49.8	48.4	47.6	48.4	53.4
Al_2O_3	4.5	16.1	15.2	13.3	19.8	18.7	17.8	18.7	18.8
MgO	14.3	3.2	5.4	7.6	15.0	18.5	20.9	18.6	12.1
CaO	19.9	4.4	26.0	30.2	15.4	13.1	12.5	13.0	12.4
Na_2O	2.7	9.8	2.8	–	–	1.3	1.2	1.3	3.3
Total	100.0	100.0	100.0	100.0	100.0	100.0	100.0	100.0	100.0

[a]S&H = composition of starting material obtained from Schosnig and Hoffer [31].
[b]W&P = composition of starting material obtained from Walter and Presnall [15].

number (cf. [23]). As mantle minerals and melts have high Mg numbers (> 70) this effect will be relatively minor.

In order to produce clinopyroxenes that cover a wide range of compositions our experimental approach was 2-fold: (1) a first set of experiments was carried out using starting glasses of compositions 80 wt% Di–20 wt% albite ($Di_{80}Ab_{20}$) and 20 wt% Di–80 wt% albite ($Di_{20}Ab_{80}$). Pressure and temperature conditions given by Blundy et al. [29] were used for experiments performed in the system $Di_{80}Ab_{20}$. Since the phase relations for the composition $Di_{20}Ab_{80}$ are only poorly known for the high pressures of this study several reconnaissance runs were carried out to constrain the liquidus phases and temperatures (for details see [30]). (2) A second set of experiments was based on previous experimental work by Walter and Presnall [15] and Schosnig and Hoffer [31]. Reported clinopyroxene and silicate melt compositions were added in desired proportions (generally 90% melt and 10% clinopyroxene) to calculate a bulk composition. Experimental run conditions given by Walter and Presnall [15], calculated with the MELTS software program of Ghiorso and Sack [32], or from reconnaissance runs were applied. The nominal (gravimetric) compositions of all starting materials used in this study are reported in Table 1.

A mixture of 1 g of each bulk composition was prepared from desired amounts of high-purity powdered oxides (SiO_2, Al_2O_3, MgO) and carbonates ($CaCO_3$, Na_2CO_3). Each mixture was ground under acetone in an agate mortar to a fine powder, decarbonated and subsequently fused in a platinum crucible at 1350°C for $\sim$10 min. Each mixture was ground and fused two or three times to obtain homogeneous glass powders. Usually about 1000 ppm of Th and 800 ppm of U were then added in nitrate solution to the glass powders using 1000 ppm AAS standard solutions (note that some starting materials were doped with about 50–200 ppm each of U and Th and that starting materials for multianvil experiments were doped with 2000 ppm U and 800 ppm Th; see Tables 3a–c for explanation). The glass powders were also doped with selected REE and yttrium (REE+Y: La, Ce, Nd, Sm, Yb, Lu and Y)

and high field strength elements (HFSE: Ti, Zr and Hf) introduced for a simultaneous study of trace element partitioning between clinopyroxene and melt, the results of which will be presented elsewhere. There are no indications that the total amount of trace elements present (< 0.5 wt% trace element oxides for all produced starting materials) has any effect on phase relations and the partitioning behaviour of U and Th. After drying and denitrification, the doped powders were again fused in a platinum crucible at 1350°C for $\sim$10 min, ground under acetone in an agate mortar and dried at 150°C. The resulting fine glass powders were used as starting materials.

Experiments were carried out at the University of Bristol using the following apparata: (1) 1–3.5 GPa experiments were carried out in 1-inch end-loaded piston cylinder apparata using $BaCO_3$ and $BaCO_3$-silica glass pressure cells, graphite furnaces, alumina spacers and WRe3/WRe25 (type D) thermocouples in alumina sleeves. No pressure correction was applied to thermocouple EMF. Based on calibrations using a number of equilibria (for details see van Westrenen et al. [12,33]) a pressure correction of −10% and −13% to the nominal pressure was applied for the $BaCO_3$ and $BaCO_3$-silica glass cells, respectively, to account for frictional losses. The samples were contained in graphite-lined Pt capsules of 3 mm outer diameter and 2–3 mm length. The graphite lining ensured that f_{O2} is at least 1.3–1.4 log units below the FMQ buffer for the conditions applied in our experiments [34]. Prior to welding, the loaded Pt capsules were heated for several minutes to 700–800°C in a furnace to ensure near-anhydrous conditions [24,35]. The capsule was protected from the thermocouple by a 0.1 mm thick Pt disc. The temperature difference between thermocouple and sample is ≤20°C based on geothermometric calibration using Di–En equilibria. To facilitate growth of large crystals, experiments were pressurised and heated to 60°C above the run temperature for 10 min. Temperature was then lowered slowly to the run temperature and held for 3–72 h, depending on the composition of the starting material (see Table 2). (2) Experiments at 5.6 and 8.1 GPa were carried out in a 'Walker-type' multianvil apparatus [36] with MgO (Ceramcast® 584)

Table 2
Experimental run conditions and products

Run	Apparatus[a]	Starting mix	P (GPa)	T (°C)	Run time (h)	Run products[b]	Notes[c]	Cpx[d]	NBO/T[e]
99 PC 11-II	EL-PC	$Di_{80}Ab_{20}$	1	1390	20	cpx+q+gl	75% melt	$Jd_2Di_{92}En_6$	1.15
99 PC 28-III	EL-PC	$Di_{80}Ab_{20}$	2	1570	4	cpx+q+gl	68% melt	$Jd_4Di_{88}En_8$	1.13
99 PC 29-II	EL-PC	$Di_{80}Ab_{20}$	2.5	1640	30	cpx+q+gl	74% melt	$Jd_6CaTs_1Di_{87}En_6$	1.20
99 PC 26-III	EL-PC	$Di_{80}Ab_{20}$	3	1665	3	cpx+gl	68% melt	$Jd_5CaTs_2Di_{84}En_9$	1.23
99 PC 24-III	EL-PC	$Di_{80}Ab_{20}$	3.5	1735	6	cpx+q	86% melt	$Jd_7CaTs_1Di_{85}En_7$	1.30
99 PC 24-IV	EL-PC	$Di_{80}Ab_{20}$	3.5	1735	5	cpx+q	80% melt	$Jd_6CaTs_1Di_{86}En_7$	1.49
30 Ab	EL-PC	$Di_{20}Ab_{80}$	3	1410	24	cpx+gl	95% melt	$Jd_{38}CaTs_5Di_{49}En_8$	0.23
99 MA 1	MA	$Di_{20}Ab_{80}$	5.6	1625	0.25	cpx+coe+q	57% melt	$Jd_{64}CaTs_7Di_{18}En_{11}$	0.22
99 MA 6	MA	$Di_{20}Ab_{80}$	5.6	1700–1650[f]	0.25	cpx+q	81% melt	$Jd_{63}CaTs_7Di_{23}En_7$	0.21
99 MA 3	MA	$Di_{20}Ab_{80}$	8.1	1685–1660[f]	0.25	cpx+coe+q	55% melt	$Jd_{69}CaTs_5Di_{18}En_8$	0.25
99 MA 7	MA	$Di_{20}Ab_{80}$	8.1	1700–1630[f]	0.25	cpx+coe+q	56% melt	$Jd_{72}CaTs_4Di_{20}En_4$	0.25
AD-1	EL-PC	S&H AD	1	1380	23	cpx+gl	82% melt	$CaTs_{21}Di_{79}$	1.04
AD-2	EL-PC	S&H AD	2	1520	40	cpx+gl	69% melt	$CaTs_{26}Di_{74}$	1.03
AD-3	EL-PC	S&H AD	3	1620	15	cpx+gl	64% melt	$CaTs_{30}Di_{70}$	1.04
AD-Na-1	EL-PC	S&H AD-Na	1	1350	55	cpx+gl	90% melt	$Jd_4CaTs_{18}Di_{78}$	0.81
AD-Na-2	EL-PC	S&H AD-Na	2	1520	67	cpx+gl	80% melt	$Jd_9CaTs_{26}Di_{65}$	0.79
AD-Na-3	EL-PC	S&H AD-Na	2.5	1550	22	cpx+gl	88% melt	$Jd_{13}CaTs_{28}Di_{59}$	0.81
AD-Na-4	EL-PC	S&H AD-Na	3	1590	6	cpx+gl	73% melt	$Jd_{13}CaTs_{30}Di_{57}$	0.81
2311-07-I	EL-PC	W&P 2311-07	1.9	1460	18	cpx+gl	66% melt	$Jd_4CaTs_{21}Di_{32}En_{43}$	0.66
2311-07-II	EL-PC	W&P 2311-07	2.3	1530	25	cpx+gl	60% melt	$Jd_5CaTs_{25}Di_{31}En_{39}$	0.67
2311-07-III	EL-PC	W&P 2311-07	3	1590	22	cpx+gt+gl+q	19% melt	$Jd_9CaTs_{25}Di_{41}En_{25}$	0.67
2701-07-I	EL-PC	W&P 2701-07	2.7	1575	25	cpx+sp+gl+q	13% melt	$Jd_5CaTs_{27}Di_{28}En_{40}$	0.59
2701-07-II	EL-PC	W&P 2701-07	3.5	1680	12	cpx+gt+q	30% melt	$Jd_8CaTs_{21}Di_{43}En_{28}$	0.92
2701-07-III	EL-PC	W&P 2701-07	3.5	1700	15	cpx+gl	85% melt	$Jd_5CaTs_{28}Di_{24}En_{43}$	0.98
122-1	EL-PC	W&P 122-1	0.9	1330	40	cpx+an+gl	50% melt	$MgTs_{14}Di_9En_{77}$	0.72
23P7	EL-PC	W&P P7	2.3	1448	24	cpx+sp+gl	27% melt	$Jd_7CaTs_{28}Di_{29}En_{36}$	0.45
30P7	EL-PC	W&P P7	3	1538	20	cpx+gl	49% melt	$Jd_7CaTs_{23}Di_{20}En_{40}$	0.66
30P10	EL-PC	W&P P10	3	1530	24	cpx+gl	60% melt	$Jd_{18}CaTs_{23}Di_{37}En_{22}$	0.38

[a] Experimental apparatus used: end-loaded piston cylinder (EL-PC) and multianvil (MA).
[b] Run products are glass (gl); quench matter (q); clinopyroxene (cpx); garnet (gt); spinel (sp); coesite (coe) and anorthite (an).
[c] Melt phase (= glass+quench matter) in wt% estimated from least squares regression of phase compositions and starting materials.
[d] Clinopyroxene composition expressed as mol% jadeite (Jd); Ca-tschermak (CaTs); diopside (Di); and enstatite (En) component.
[e] Degree of depolymerisation (NBO/T) of melts calculated from melt composition using the method of Mysen et al. [47].
[f] Variation in T due to thermal gradient in multianvil capsules.

octahedra with an edge length of 18 mm, unta-pered $LaCrO_3$ furnaces and ZrO_2 sleeves between octahedron and furnace. Temperature was moni-tored by an axial W–Re thermocouple in an alu-mina sleeve. No pressure correction was applied to thermocouple EMF. The samples were con-tained in welded Pt capsules of 1.8 mm outer di-ameter and typically 3 mm length. The temper-ature difference between thermocouple and sample in this assembly is no more than $\pm 20°C$ based on calibration using two thermocouples. Samples were taken directly to run temperature and run times were ≤ 15 min. Experimental run conditions of all experiments reported in this study are given in Table 2.

3. Analytical techniques

The major element chemistry of minerals and silicate glasses of all experiments was determined on carbon-coated polished mounts at the Univer-sity of Bristol using a Jeol JXA-8600 electron mi-croprobe analyser (EMPA) in wavelength disper-sive mode. Accelerating voltage and beam current were 15 kV and 15 nA, respectively. For mineral analysis, beam diameter was 1 μm, while a slightly defocussed beam of 5–10 μm diameter was used for silicate glass analysis to minimise migration of sodium. Standards used for calibration were albite (Na), wollastonite (Ca, Si), olivine (Mg) and spinel (Al). All raw data were reduced using a ZAF correction scheme. Typical 1σ precision is generally better than 2% for > 5 oxide wt%, 4% for 5–3 oxide wt%, and 6% for < 3 oxide wt%. Analyses of secondary standards (Di and KK1 kaersutite) were consistently within 2σ of pub-lished values.

All trace element concentrations were deter-mined on Au-coated mounts by secondary ion mass spectrometry (SIMS) using the Cameca IMS-4f ion microprobe at the University of Edin-burgh. If possible, SIMS and EMPA measure-ments were performed at the same spot. The pri-mary beam was nominally 10 keV O^- ions with a sample current of 6–12 nA, corresponding to a spatial resolution of ~ 30–50 μm. The secondary ion accelerating voltage was 4500 V with an offset

of 75 V and energy window of ± 20 eV to reduce molecular ion transmission. Calibration was per-formed under similar operating conditions using NIST SRM 610 glass, adopting the NIST recom-mended values of 457.2 ppm for Th and 461.5 ppm for U (in reality the exact values adopted have no bearing on our partition coefficients which, of course, are ratios). ^{238}U and ^{232}Th were measured and ratioed to ^{30}Si as determined by electron microprobe. Mass 130.5 was used to monitor background; all analyses reported here have zero background counts. Count times were adjusted so as to ensure a statistical precision of better than 5% relative for all measured isotopes. Accuracy of SIMS analyses was assessed by ana-lyzing regularly a set of secondary standards (Kil-bourne Hole clinopyroxene KH1, San Carlos cli-nopyroxene SC8804, Madagascan garnet). Comparison of the results obtained over a 5 yr period with independently determined and pub-lished analyses of these materials indicates that accuracy is better than 15% and there is no sys-tematic variation in ion yield between silicate glasses and mantle minerals.

4. Experimental results

Experimental run products are listed in Table 2. In $Di_{80}Ab_{20}$ and $Di_{20}Ab_{80}$ systems experimental run products were 14–32% clinopyroxene coexist-ing with 68–86% homogeneous glass and spheru-litic quench matter (see Fig. 2a). In the 5–8.1 GPa runs, clinopyroxene is joined by coesite as a stable phase. Clinopyroxenes were generally euhedral and varied in length between 50 and several 100 μm. In S and H experiments (starting materials after Schosnig and Hoffer [31]) run products were 10–36% large euhedral clinopyroxene up to 500 μm in size surrounded by 64–90% clear ho-mogeneous glass (see Fig. 2b). In W&P experi-ments (starting materials after Walter and Pres-nall [15]) the quenched assemblages can be divided in two groups: (a) in the first group run products were 15–40% clinopyroxene coexisting with 60–85% clear homogeneous glass. Clinopyr-oxenes in these runs are euhedral to subhedral and 100–200 μm in size; (b) in the second group
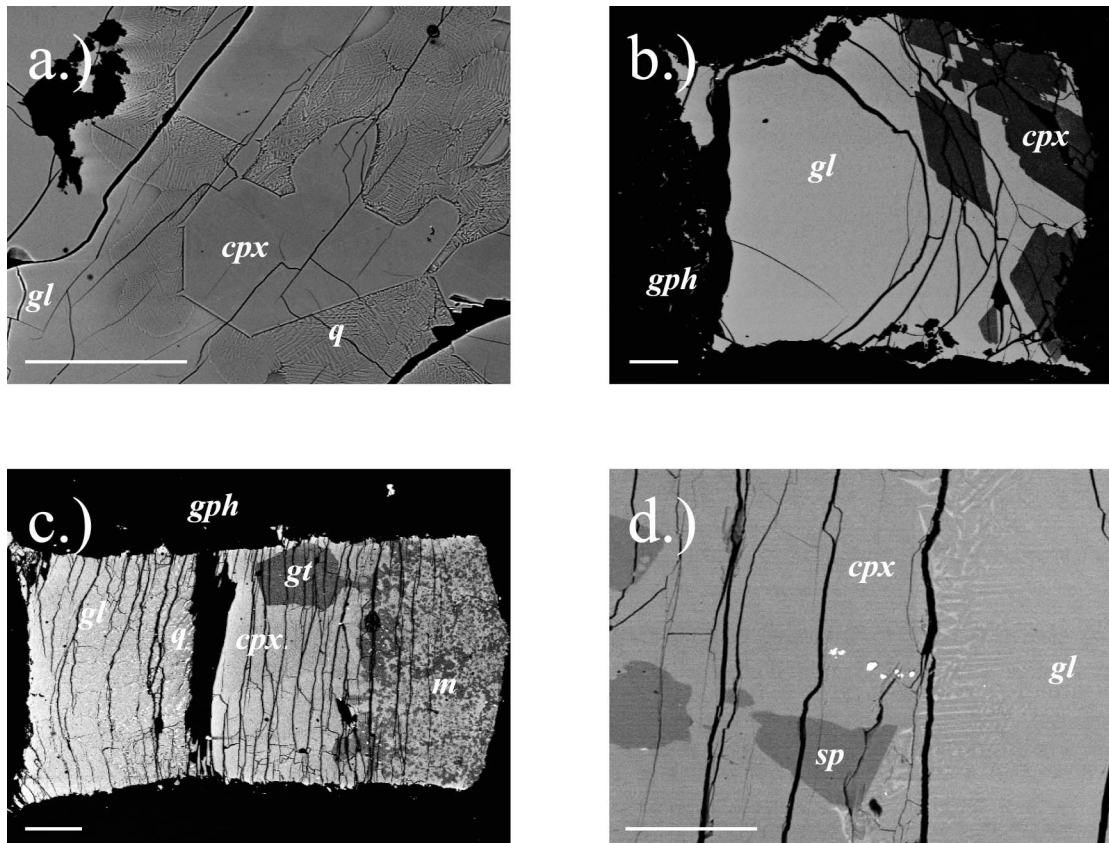
Fig. 2. Secondary electron photomicrographs of typical experimental run products (see Table 2 for run conditions): (a) 1 GPa run 99PC11-II showing euhedral clinopyroxene (*cpx*) in matrix of spherulitic quench matter (*q*) and homogeneous glass (*gl*). (b) 1 GPa run AD-1 showing large euhedral clinopyroxene (*cpx*) in homogeneous glass matrix (*gl*) surrounded by graphite lining (*gph*). (c) 3.5 GPa run 2701-07-II showing an interlocking matrix of fine grained clinopyroxene and garnet at the base of the capsule (*m*), subhedral clinopyroxene (*cpx*) and euhedral garnet (*gt*) coexisting with a homogeneous glass (*gl*) and spherulitic quench matter (*q*) surrounded by graphite lining (*gph*). (d) 2.7 GPa run 2701-07-I showing subhedral clinopyroxene (*cpx*) and spinel (*sp*) coexisting with homogeneous glass (*gl*) and a spherulitic quench rim at the crystal–melt interface. Scale bar in each photomicrograph is 200 μm.

run products were 13–50% homogeneous glass ± sperulitic quench matter and variable proportions of clinopyroxene ± garnet or spinel. An interlocking matrix of fine grained clinopyroxene and garnet typically forms near the base of the capsule, while large subhedral clinopyroxene of up to 300 μm ± euhedral garnet or subhedral spinel occurs at the melt interface near the top of the capsule (see Fig. 2c). Only crystals close to this interface were analysed. Spherulitic quench matter typically forms rims at crystal–melt interfaces (see Fig. 2d).

Major element analyses of all experimental run products are listed in Tables 3a–c. The small stan- dard deviation (S.D.) for each of the analysed glasses demonstrates that they are chemically ho- mogeneous. Spherulitic quench mats inevitably show local heterogeneity leading to problems dur- ing EMPA [29]. Thus, the larger S.D. values for some of the analysed quench mats (for example MgO in runs 99PC24-III, 99MA1 and 2701-07-II) are likely due to analytical uncertainty because of the small number of points analysed rather than reflecting chemical inhomogeneity. Observed melt chemistry, expressed as degree of depolymerisa- tion of the melt (Table 2), shows a large variation from fully polymerised (NBO/T values about 0.2

Table 3a
Chemical composition of experimental run products and calculated partition coefficients[a]

Run	99 PC 11-II	99 PC 28-III	99 PC 29-II	99 PC 26-III	99 PC 24-III	99 PC 24-IV[e]	30 Ab	99 MA 1	99 MA 6	99 MA 3	99 MA 7
System	$Di_{80}Ab_{20}$	$Di_{80}Ab_{20}$	$Di_{80}Ab_{20}$	$Di_{80}Ab_{20}$	$Di_{80}Ab_{20}$	$Di_{80}Ab_{20}$	$Di_{20}Ab_{80}$	$Di_{20}Ab_{80}$	$Di_{20}Ab_{80}$	$Di_{20}Ab_{80}$	$Di_{20}Ab_{80}$
P (GPa)	1	2	2.5	3	3.5	3.5	3	5.6	5.6	8.1	8.1
T (°C)	1390	1570	1640	1665	1735	1735	1410	1625	1700–1650	1685–1660	1700–1630
wt%	**Pyroxene**										
n[b]	16	6	11	21	11	49		21	10	12	19
SiO_2	55.57 (25)	55.69 (27)	55.26 (34)	55.42 (25)	55.90 (22)	55.78 (24)	56.65 (32)	58.28 (49)	56.36 (48)	58.59 (40)	57.26 (49)
Al_2O_3	0.52 (6)	1.27 (4)	1.73 (15)	2.28 (24)	2.11 (11)	1.89 (23)	11.60 (9)	19.61 (28)	18.69 (25)	19.54 (44)	20.05 (42)
MgO	19.84 (30)	19.70 (27)	18.91 (20)	19.18 (22)	18.82 (8)	19.23 (27)	12.12 (43)	5.93 (30)	7.07 (31)	5.49 (27)	5.55 (64)
CaO	23.95 (21)	23.08 (19)	22.96 (12)	22.54 (17)	22.55 (17)	22.68 (27)	14.51 (4)	7.03 (25)	8.17 (25)	6.17 (33)	6.66 (35)
Na_2O	0.25 (3)	0.63 (5)	0.86 (8)	0.78 (6)	1.01 (5)	0.90 (11)	5.64 (9)	9.68 (26)	9.34 (25)	10.45 (23)	10.88 (46)
Total	100.13 (43)	100.37 (38)	99.72 (42)	100.20 (33)	100.39 (33)	100.47 (37)	100.52 (20)	100.53 (31)	99.65 (30)	100.27 (33)	100.40 (47)
ppm											
n[b]	7	5	6	6	3	4		2	2	3	2
U	1.7 (6)	1.4 (1)	2.3 (9)	1.1 (1)	2.4 (7)	1.3 (3)	0.26 (8)	2.08 (36)	2.78 (49)	1.39 (19)	1.59 (9)
Th	2.5 (6)	2.4 (4)	2.9 (8)	1.5 (1)	3.1 (7)	1.8 (5)	0.24 (12)	0.83 (23)	0.95 (24)	0.35 (13)	0.51 (6)
U/Th[c]	0.67 (11)	0.61 (10)	0.77 (8)	0.73 (2)	0.75 (9)	0.75 (17)	1.15 (23)	2.60 (27)	2.98 (25)	4.28 (88)	3.16 (23)
wt%	**Glass**										
n[b]	23	5	10	13	10	36		16	18	11	4
SiO_2	58.62 (51)	58.99 (18)	57.87 (56)	56.94 (27)	57.84 (103)	56.94 (76)	65.73 (20)	70.35 (40)	66.98 (41)	69.92 (27)	68.27 (45)
Al_2O_3	6.09 (44)	6.06 (7)	5.62 (31)	6.61 (9)	5.05 (30)	4.16 (26)	16.22 (21)	11.86 (45)	14.17 (22)	11.19 (22)	9.83 (17)
MgO	12.55 (54)	11.95 (17)	12.55 (89)	13.90 (21)	14.08 (147)	16.13 (93)	3.38 (19)	2.10 (26)	2.50 (8)	2.21 (5)	1.22 (8)
CaO	18.32 (42)	18.16 (15)	18.83 (54)	19.37 (19)	19.57 (63)	21.21 (38)	4.64 (16)	4.38 (12)	4.46 (16)	4.57 (4)	4.71 (9)
Na_2O	3.21 (51)	3.94 (9)	3.19 (30)	2.21 (16)	2.60 (57)	1.82 (20)	9.60 (7)	8.74 (24)	8.95 (17)	9.08 (14)	9.36 (18)
Traces[d]								1.16	1.12	1.55	4.53
Total	98.79 (50)	99.10 (11)	98.06 (33)	99.03 (36)	99.14 (35)	100.26 (38)	99.57 (17)	99.10 (29)	98.18 (20)	98.46 (14)	98.72 (19)
ppm											
n[b]	6	4	6	4	6	4		2	2	2	2
U	1030 (83)	1797 (109)	1458 (108)	1026 (110)	1828 (239)	1230 (357)	60 (1)	3835 (295)	1790 (50)	2435 (235)	5010 (580)
Th	1153 (60)	1803 (76)	1418 (105)	1020 (86)	1712 (206)	1254 (283)	61.8 (8)	1530 (130)	715 (27)	970 (90)	2005 (245)
U/Th[c]	0.89 (4)	0.99 (5)	1.03 (1)	1.00 (3)	1.07 (2)	1.02 (7)	0.974 (6)	2.51 (2)	2.50 (2)	2.51 (1)	2.50 (2)
D_U	0.0017 (6)	0.00078 (9)	0.0016 (6)	0.00107 (1)	0.0013 (4)	0.0011 (4)	0.0044 (14)	0.00054 (15)	0.0016 (4)	0.00057 (10)	0.00025 (4)
D_{Th}	0.0022 (5)	0.0013 (2)	0.0020 (6)	0.00147 (1)	0.0018 (4)	0.0014 (5)	0.0039 (19)	0.00054 (10)	0.0013 (5)	0.00036 (14)	0.00032 (4)
D_U/D_{Th}	0.75 (13)	0.61 (10)	0.75 (8)	0.73 (3)	0.71 (9)	0.74 (17)	1.18 (24)	1.04 (15)	1.19 (15)	1.71 (43)	1.27 (13)

[a] Units in parentheses are 1 S.D. of replicate analyses in terms of least units cited. Thus 55.57 (25) should be read as 55.57 ± 0.25.
[b] Number of analyses by EMPA (for major elements) and SIMS (for U and Th).
[c] Note that the U/Th ratio was measured at each point and has a higher precision than the absolute U and Th concentrations.
[d] A limited selection of trace elements were analysed by EMPA for these melts. See Chamoro-Perez et al. [30] for explanation.
[e] Duplicate of experiment 99 PC 24-III.

Table 3b
(See Table 3a for explanations)

Run	AD-1	AD-2	AD-3	AD-Na-1	AD-Na-2	AD-Na-3	AD-Na-4
System	S&H	S&H	S&H	S&H	S&H	S&H	S&H
P (Gpa)	1	2	3	1	2	2.5	3
T (°C)	1380	1520	1620	1350	1520	1550	1590
wt%	Pyroxene						
n^b	11	9	24	77	59	16	21
SiO_2	49.88 (23)	47.74 (35)	47.26 (49)	50.64 (42)	48.81 (28)	48.33 (51)	47.18 (24)
Al_2O_3	10.00 (22)	12.36 (25)	14.00 (18)	9.68 (40)	14.50 (46)	16.20 (30)	17.17 (17)
MgO	14.72 (13)	13.94 (14)	12.96 (24)	14.66 (24)	12.15 (23)	10.95 (19)	10.09 (9)
CaO	26.23 (14)	26.08 (15)	26.16 (35)	25.24 (17)	24.21 (17)	23.11 (28)	23.37 (17)
Na_2O	0.02 (1)	0.03 (2)	0.04 (2)	0.54 (5)	1.35 (10)	1.87 (7)	1.78 (4)
Total	100.85 (27)	100.16 (43)	100.42 (111)	100.76 (60)	101.03 (40)	100.46 (96)	99.59 (28)
ppm							
n^b	6	5	5	6	5	5	5
U	3.5 (6)	2.8 (7)	1.2 (1)	2.1 (6)	1.9 (3)	1.0 (2)	1.1 (3)
Th	5.8 (10)	5.9 (20)	1.7 (2)	4.0 (15)	3.3 (4)	1.5 (5)	1.6 (5)
U/Th^c	0.60 (3)	0.51 (10)	0.73 (7)	0.56 (5)	0.59 (5)	0.66 (7)	0.65 (6)
wt%	Glass						
n^b	43	22	24	21	103	80	21
SiO_2	48.33 (19)	48.18 (31)	48.96 (41)	50.44 (40)	51.32 (20)	51.20 (22)	51.20 (14)
Al_2O_3	14.24 (12)	13.70 (9)	13.25 (11)	15.81 (14)	15.73 (12)	15.71 (9)	15.03 (7)
MgO	6.08 (6)	4.68 (8)	4.50 (6)	4.38 (5)	3.88 (6)	4.59 (5)	3.27 (8)
CaO	30.82 (18)	31.92 (13)	32.39 (17)	26.06 (20)	26.31 (22)	26.38 (14)	27.20 (13)
Na_2O	0.06 (2)	0.03 (2)	0.04 (2)	3.07 (17)	3.04 (6)	2.38 (6)	2.98 (7)
Total	99.53 (33)	98.51 (39)	99.14 (50)	99.76 (68)	100.28 (36)	100.26 (33)	99.68 (21)
ppm							
n^b	6	6	6	6	6	6	6
U	503 (29)	770 (16)	785 (9)	492 (35)	704 (31)	475 (4)	604 (32)
Th	730 (37)	1065 (15)	1089 (15)	724 (42)	999 (48)	701 (6)	891 (58)
U/Th^c	0.69 (2)	0.72 (1)	0.72 (1)	0.68 (1)	0.705 (4)	0.677 (2)	0.678 (8)
D_U	0.0070 (13)	0.0037 (9)	0.0015 (1)	0.004 (1)	0.0027 (4)	0.0021 (4)	0.0018 (5)
D_{Th}	0.0080 (15)	0.0055 (19)	0.0015 (1)	0.005 (2)	0.0033 (5)	0.0021 (6)	0.0018 (5)
D_U/D_{Th}	0.87 (5)	0.70 (13)	1.01 (9)	0.82 (7)	0.84 (8)	0.97 (11)	0.96 (9)

in $Di_{20}Ab_{80}$ runs) to depolymerised melts (NBO/T of 1.2 in $Di_{80}Ab_{20}$ runs). However, no correlation between D_U/D_{Th} or D_{Th} values and NBO/T is observed and experiments with quite different NBO/T values show the same D_U/D_{Th} and D_{Th} values.

Although homogeneous clinopyroxene crystals are notoriously difficult to grow, the majority of experimentally produced clinopyroxenes reported in this study are remarkably homogeneous. With a few exeptions, the observed chemical variation even for species showing slow interdiffusion is insignificant. For example, the greatest observed variation in Al_2O_3 is ∼12% relative (for pigeonite in run W&P 122-1), but is generally ≤6% relative

for the majority of clinopyroxenes. The average observed variation in Al_2O_3 is only ∼4% relative. Moreover, for ∼60% of the experimentally produced clinopyroxenes the observed variation in Al_2O_3 is below the analytical precision. This also holds true for garnets produced in runs W&P 2311-07-III and W&P 2701-07-II, and spinel in runs W&P 2701-07-I and W&P 23P7. In addition, no systematic or complementary major element zonation is observed for clinopyroxene, garnet and spinel.

The homogeneity of almost all run products and the close match between clinopyroxene major and trace element compositions in our duplicated experiment at 3.5 GPa/1735°C (99PC24-III/

Table 3c
(See Table 3a for explanations)

Run	2311-07-I	2311-07-II	2311-07-III	2701-07-I	2701-07-II	2701-07-III	23P7	30P7	30P10	122-1	2311-07-III	2701-07-II
System	W&P	W&P	W&P	W&P	W&P	W&P	W&P	W&P	W&P	W&P	W&P	W&P
P (Gpa)	1.9	2.3	3	2.7	3.5	3.5	2.3	3	3	0.9	3	3.5
T (°C)	1460	1530	1590	1575	1680	1700	1448	1538	1530	1330	1590	1680
wt%	Pyroxene										Garnet	
n[b]	11	49	11	8	11	11	23	27	22	7	10	11
SiO_2	50.49 (41)	49.65 (64)	50.70 (22)	49.81 (53)	51.07 (22)	48.37 (28)	51.20 (40)	49.16 (32)	48.52 (17)	55.23 (36)	43.54 (16)	43.52 (13)
Al_2O_3	11.28 (58)	13.28 (102)	14.35 (7)	14.51 (68)	12.04 (27)	14.64 (11)	15.59 (25)	15.02 (18)	17.87 (7)	7.19 (86)	25.30 (14)	24.72 (11)
MgO	22.84 (78)	21.21 (73)	17.17 (10)	20.92 (72)	18.98 (24)	21.53 (7)	14.50 (38)	18.95 (51)	18.55 (4)	35.39 (51)	24.72 (52)	24.08 (7)
CaO	14.07 (67)	15.00 (48)	17.65 (10)	14.74 (43)	16.99 (19)	13.78 (10)	15.92 (8)	14.94 (22)	14.09 (6)	2.54 (7)	6.60 (17)	7.1 (9)
Na_2O	0.63 (3)	0.67 (4)	1.40 (3)	0.74 (3)	1.24 (3)	0.72 (2)	2.62 (8)	1.09 (9)	1.11 (6)	0.01 (1)	0.02 (2)	–
Total	99.31 (45)	99.81 (48)	101.27 (32)	100.72 (26)	100.32 (32)	99.04 (30)	99.83 (24)	99.16 (26)	100.14 (8)	100.36 (35)	100.18 (37)	99.42 (16)
ppm												
n[b]	4	5	5	4	5	6	6	5	6	2	5	3
U	12.3 (14)	17.0 (8)	15.1 (8)	9.5 (16)	9.30 (19)	7.6 (12)	3.58 (20)	1.43 (16)	0.58 (3)	0.82 (15)	45.9 (103)	52.6 (58)
Th	9.6 (18)	13.9 (9)	13.9 (7)	10.5 (21)	12.2 (25)	7.7 (14)	3.64 (40)	1.07 (21)	0.51 (6)	0.33 (12)	9.2 (26)	17.8 (24)
U/Th[c]	1.31 (12)	1.22 (3)	1.08 (2)	0.91 (3)	0.76 (4)	0.98 (5)	0.98 (24)	1.35 (13)	1.15 (10)	2.49 (41)	5.1 (3)	2.96 (8)
wt%	Glass											
n[b]	11	47	41	35	21	11	42	51	49	11	41	21
SiO_2	49.36 (31)	48.79 (27)	51.77 (25)	48.85 (32)	48.81 (69)	47.25 (32)	50.50 (13)	48.33 (23)	55.72 (18)	49.57 (34)	51.77 (25)	48.81 (69)
Al_2O_3	21.09 (14)	21.60 (18)	20.88 (11)	21.28 (16)	17.15 (58)	18.35 (56)	22.50 (11)	21.32 (34)	20.46 (53)	19.32 (11)	20.88 (11)	17.15 (58)
MgO	14.59 (9)	15.05 (13)	12.62 (7)	15.00 (15)	16.85 (116)	20.24 (31)	11.01 (16)	15.1 (18)	8.39 (26)	13.83 (8)	12.62 (7)	16.85 (116)
CaO	12.44 (6)	12.45 (9)	12.84 (8)	12.30 (9)	14.20 (71)	12.47 (28)	11.11 (24)	11.86 (19)	10.32 (33)	15.52 (11)	12.84 (8)	14.20 (71)
Na_2O	1.83 (4)	1.75 (4)	2.23 (4)	1.70 (5)	1.48 (14)	0.91 (6)	2.35 (4)	1.57 (7)	3.60 (10)	0.11 (2)	2.23 (4)	1.48 (14)
Total	99.31 (48)	99.64 (51)	100.34 (38)	99.13 (56)	98.49 (170)	99.22 (62)	97.47 (14)	98.18 (20)	98.49 (28)	98.35 (39)	100.34 (38)	98.49 (170)
ppm												
n[b]	5	6	6	5	7	6	6	6	6	2	6	7
U	1224 (130)	1333 (27)	2263 (57)	2363 (216)	2227 (925)	494 (59)	211 (5)	211 (54)	60 (1)	1479 (204)	2263 (57)	2227 (925)
Th	1261 (152)	1342 (21)	2223 (47)	2798 (129)	2449 (904)	660 (72)	228 (3)	187 (39)	69 (1)	1685 (225)	2223 (47)	2449 (904)
U/Th[c]	0.97 (2)	0.993 (5)	1.018 (5)	0.84 (4)	0.89 (5)	0.75 (2)	0.93 (10)	1.12 (7)	0.865 (4)	0.88 (1)	1.018 (5)	0.89 (5)
D_U	0.0101 (16)	0.0127 (7)	0.0067 (4)	0.0040 (8)	0.0042 (19)	0.015 (3)	0.017 (6)	0.0068 (19)	0.0097 (5)	0.00055 (13)	0.020 (5)	0.024 (10)
D_{Th}	0.0076 (17)	0.0104 (7)	0.0063 (4)	0.0037 (8)	0.0050 (21)	0.012 (3)	0.016 (11)	0.0057 (16)	0.0074 (10)	0.00019 (7)	0.0041 (12)	0.0073 (29)
D_U/D_{Th}	1.34 (12)	1.23 (3)	1.06 (2)	1.08 (6)	0.85 (6)	1.31 (7)	1.05 (26)	1.21 (14)	1.33 (13)	2.83 (47)	4.98 (29)	3.32 (21)

99PC24-IV) provide compelling evidence for equilibrium. Furthermore, all crystals and melts produced are essentially unzoned with respect to the REE+Y and HFSE added (see above) and measured partition coefficients for these elements follow the parabolic dependence on ionic radius predicted for equilibrium partitioning by Nagasawa [37] and Brice [38]. We therefore conclude that our experiments offer a very close approximation to equilibrium.

Clinopyroxenes in the NCMAS system are quarternary solid solutions involving the Di component (Di = $CaMgSi_2O_6$), the En component (En = $Mg_2Si_2O_6$), the Jd component (Jd = $NaAlSi_2O_6$), and the CaTs component (CaTs = $CaAl_2SiO_6$). Clinopyroxene compositions from our experiments recalculated into endmember mole fractions are given in Table 2. Mole fractions are calculated from six-oxygen structural formulas using the following expressions: $X_{En} = 1 - Ca - Na$, $X_{Jd} = Na$, $X_{CaTs} = (Al - Na)/2$, and $X_{Di} = 1 - X_{En} - X_{Jd} - X_{CaTs}$. Mole fraction endmember components for pigeonite (run W&P 122-1) are calculated from: $X_{Di} = Ca$, $X_{Jd} = Na$, $X_{MgTs} = (Al - Na)/2$, and $X_{En} = 1 - X_{Di} - X_{Jd} - X_{MgTs}$ where MgTs is the component $MgAl_2SiO_6$.

Experimentally produced clinopyroxenes show a wide range of compositions from diopsidic, jadeiitic and Ca-tschermakitic to En-rich clinopyroxenes. In $Di_{80}Ab_{20}$ runs clinopyroxenes are high-Ca, low-Al Di: Jd and En content increase and Di content decreases with increasing pressure. In $Di_{20}Ab_{80}$ runs clinopyroxenes are high-Na, high-$Al^{[VI]}$ jadeiitic clinopyroxenes: Jd content strongly increases with increasing pressure from 38 mol% at 3 GPa to 72 mol% at 8.1 GPa. In S&H systems clinopyroxenes are high-Ca, high-CaTs clinopyroxenes: CaTs content increases with increasing pressure, from 18 mol% at 1 GPa to 30 mol% at 3 GPa. In W&P systems clinopyroxenes are low-Ca, high-Al En-rich clinopyroxenes: compositions range from $Jd_9CaTs_{25}Di_{41}En_{25}$ at 3 GPa/ 1590°C to $Jd_5CaTs_{28}Di_{24}En_{43}$ at 3.5 GPa/1700°C. Euhedral to subhedral clinopyroxenes produced in run W&P 122-1 are low-Ca, En-rich pigeonites ($MgTs_{14}Di_9En_{77}$).

Large euhedral garnets (up to 600 μm in diameter) produced in runs W&P 2311-07-III and W&P 2701-07-II fall on the pyrope–grossular join and are pyropic in composition ($Py_{85}Grs_{15}$ and $Py_{83}Grs_{17}$, respectively).

5. U and Th partitioning

U and Th contents of all experimental run products as determined by SIMS and partition coefficients for clinopyroxene and garnet are given in Tables 3a–c. Some crystalline phases exhibit a slight zoning in U and Th, but the U/Th ratio is essentially constant across the crystals. D_U/D_{Th} values calculated from the ratio of U/Th values of clinopyroxene and melt have a higher precision than D_U/D_{Th} values calculated from absolute values of D_U and D_{Th} [19] and are reported separately in Tables 3a–c. Note that the U/Th ratio of the melt phases is below unity for the majority of our experiments and hence contamination by concurrently analysed glass during SIMS analyses of clinopyroxene can only shift D_U/D_{Th} ratios closer to or even below unity. Hence D_U/D_{Th} values for these experiments are minimum values.

In Fig. 3 the results of this study are compared with the predicted D_U/D_{Th} values calculated from Eqs. 2–4. The solid line is calculated using ionic radii of U and Th from Shannon [25] (1.00 Å and
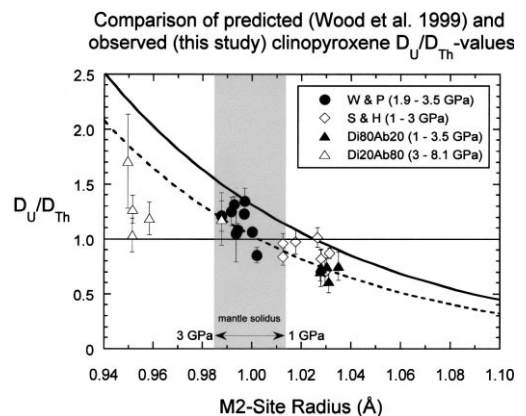

Fig. 3. Predicted D_U/D_{Th} values compared with the results of this study. For high pressure clinopyroxenes on the mantle solidus (W&P) D_U/D_{Th} is >1 at values of M2 site radius <1.0 Å. Error bars (shown if bigger than symbols) are ±1 S.D.

1.05 Å, respectively) and the dashed line is calculated using the revised ionic radii of U and Th from Wood et al. [19] (0.983 Å and 1.041 Å, respectively). Shaded area depicts the predicted decrease of M2 site radii for mantle solidus clinopyroxenes from 1.013 Å at 1 GPa to 0.985 Å at 3 GPa. The striking features of Fig. 3 are that: (1) within error all data (except some of the very Jd-rich experiments in the system $Di_{20}Ab_{80}$ and one experiment in the system W&P) plot on the predicted trend for D_U/D_{Th}; and (2) that D_U/D_{Th} crosses over from values < 1 at M2 site radii > 1.00 Å (diopsidic and Ca-tschermakitic clinopyroxenes in systems $Di_{80}Ab_{20}$ and S&H, respectively) to values > 1 at M2 site radii < 1.00 Å (high pressure Ca-poor, Al-rich pyroxenes on the NCMAS mantle solidus, system W&P, and jadeiitic clinopyroxenes, system $Di_{20}Ab_{80}$). The clear implication of Fig. 3 is that for mantle solidus clinopyroxenes with M2 site radii < 1.00 Å the clinopyroxene–melt values of D_U/D_{Th} are > 1.

The absolute values of D_U and D_{Th} vary by two orders of magnitude (between 3×10^{-4} for clinopyroxenes with $Al^{[IV]} < 0.025$ apfu and 1.3×10^{-2} for aluminous clinopyroxenes with $Al^{[IV]} > 0.125$ apfu) and are in excellent agreement with values from the literature [7–10,19,26]. Because the partitioning behaviour of Th is, unlike that of U, independent of oxygen fugacity [10,19] we will focus on the partitioning behaviour of Th in order to develop a simple thermodynamic model of Th partitioning between clinopyroxene and silicate melt that incorporates all partitioning data reported in the literature.

The strong correlation between absolute D_{Th} values and tetrahedrally coordinated Al was first demonstrated by Lundstrom et al. [10]. Lundstrom et al. suggested that this correlation is caused by the fact that only tetrahedral Al (and not octahedral Al) can effectively charge balance Th^{4+}, e.g. as $ThMgAl_2O_6$. This is supported by the low D_{Th} values for the jadeiitic clinopyroxenes in the system $Di_{20}Ab_{80}$, where Al is almost exclusively octahedrally coordinated. However, the dependence of absolute D_{Th} values on $Al^{[IV]}$ holds only up to a 'threshold' $Al^{[IV]}$ content of ~ 0.125 apfu; at higher $Al^{[IV]}$ contents D_{Th} is relatively insensitive to $Al^{[IV]}$ (see figure 6 in [39]). Wood

and Blundy [39] ascribe the $Al^{[IV]}$ dependence of D_{Th} to the availability of clinopyroxene M2 sites with the appropriate 4+ charge, and the electrostatic energy penalty for inserting Th onto a site with lower charge.

An alternative way of looking at Th partitioning is in terms of intensive variables. Fig. 4 shows that temperature also has a marked effect on Th partitioning. Linear regression of $RT \ln D_{Th}$ versus temperature for all high pressure data yields a correlation coefficient of 0.68 and an entropy of fusion of 92 J mol^{-1} K^{-1}. This value is in good agreement with values for Di (83 J mol^{-1} K^{-1} [40]), REE-pyroxene (66 J mol^{-1} K^{-1} [23]) and Jd (65 J mol^{-1} K^{-1} [29]). Note that all near-isobaric, polythermal data plot in an array close to the regression line. Isothermal data from one atmosphere experiments [7,8,10] reflect the strong influence of crystal composition (i.e. $Al^{[IV]}$ content [10,39]; see above) in controlling Th partitioning. However, the higher pressure data on which the regression is based consistently have more than 0.125 $Al^{[IV]}$ apfu (except those of Beattie [7]) and are therefore insensitive to Al content. As mantle clinopyroxenes also have elevated Al contents it is these compositions which are of the greatest interest to us in developing our models.

Clearly both intensive variables and phase compositions control partitioning, and should be included in a comprehensive model. Such a model is
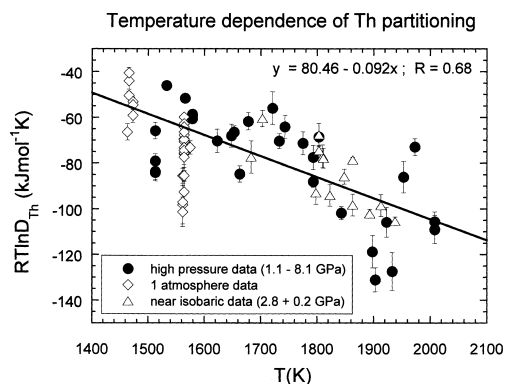

Fig. 4. $RT \ln D_{Th}$ as a function of temperature. Note the marked temperature dependence of $RT \ln D_{Th}$ values. Linear regression of all high pressure data gives $RT \ln D_{Th} = 80.46 - 0.092T$ [K] and a correlation coefficient of 0.68. Error bars (shown if bigger than symbols) are ± 1 S.D.

currently under development, but is beyond the scope of this paper. Our goal here is to parameterise Th (and U) partitioning in a thermodynamically valid way, so that our data can be applied to problems of mantle melting. To this end we have used the melting curve approach of Wood and Blundy [23] wherein partitioning is discussed in terms of the free energy of fusion of a fictive component containing the trace element(s) of interest.

Following Lundstrom et al. [10] and Wood et al. [19] we consider that the most plausible charge-balanced clinopyroxene species is $ThMgAl_2O_6$. Hence Th partitioning is controlled by the fusion reaction:

$$ThMgAl_2O_6 \ (pyroxene) = ThMgAl_2O_6 \ (melt) \tag{5}$$
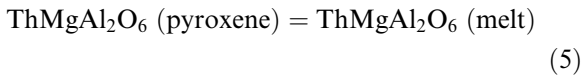
For this reaction the equilibrium constant for Eq. 5 K_5 is related to the entropy (ΔS_f), enthalpy (ΔH_f) and volume (ΔV_f) of fusion by:

$$-RT \ln K_5 = \Delta H_f - T\Delta S_f + P\Delta V_f \tag{6}$$

In order to formulate K_5 we require activity–composition relationships for $ThMgAl_2O_6$ in crystal and melt. Following Wood and Blundy [23] we use a mixing-on-sites model for the crystal, assuming complete short-range order between M and T sites, thus the activity of $ThMgAl_2O_6$ in clinopyroxene is given by:

$$\alpha_{ThMgAl_2O_6}^{Cpx} = X_{Th}^{M2} \gamma_{Th}^{M2} X_{Mg}^{M1} \gamma_{Mg}^{M1} \tag{7}$$

where the X and γ terms denote mole fraction and activity coefficients, respectively, for the species (subscript) and site (superscript) of interest. γ_{Mg}^{M1} is given by $\exp(W_{Mg-Al}/RT)$ where W_{Mg-Al} is a Mg–Al Margules binary interaction parameter for the M1 site. Based on available experimental data W_{Mg-Al} has a value of ~ 7.5 kJ mol^{-1} [41] and this value has been adopted in this study. Note that this value of W_{Mg-Al} is sufficiently small that its exclusion would have very little bearing on our model. The value of γ_{Th}^{M2} can be readily calculated from the lattice strain model, in terms of the energy required to insert Th into a lattice site of radius r_0:

$$\gamma_{Th}^{M2} = \exp\left(\frac{\Delta G_{strain}^{Th-M2}}{RT}\right) =$$

$$\exp\left[\frac{4\pi E_{M2}^{4+} N_A}{RT}\left[\frac{r_0}{2}(r_{Th}-r_0)^2 + \frac{1}{3}(r_{Th}-r_0)^3\right]\right] \tag{8}$$

For the melt, in an analogous fashion to Wood and Blundy [23], we adopt a model of ideal mixing of six-oxygen $[Al_2O_6]^{6-}$ units [23]:

$$\alpha_{ThMgAl_2O_6}^{melt} = X_{Th}^{6ox} X_{Mg}^{6ox} \tag{9}$$

Fitting all available 71 D_{Th} values (27 from this study and 44 from the literature) and subsequently excluding five outliers gives the following expression that describes Th partitioning between clinopyroxene and silicate melt from temperature, pressure and crystal and melt chemistry:

$$RT \ln D_{Th} \gamma_{Th}^{M2} X_{Mg}^{M1} \gamma_{Mg}^{M1} / X_{Mg}^{L} =$$

$$214.79 - 0.757T + 16.42P - 1.50P^2 \tag{10}$$

where R is the gas constant (0.008314 kJ mol^{-1}), T is in K and P is in GPa, and X_{Mg}^{X1} and X_{Mg}^{L} are the mole fractions of Mg on the clinopyroxene M1 position and in the liquid, calculated on a six-oxygen basis, respectively. The goodness of the fit is $\sigma_{fit} = 3.0$ kJ mol^{-1}. In Fig. 5 observed D_{Th} values are plotted as a function of predicted (from Eq. 10) D_{Th} values. Given the fact that D_{Th} values vary by two orders of magnitude, the agreement between observed D_{Th} values and those predicted from Eq. 10 is reasonable. The only persistent outliers are the high pressure data of Beattie [7], and some one atmosphere data. With respect to the latter it is clear that our attempt to account for all crystal chemical dependence of partitioning using Al–Mg interaction on M1 is inadequate. However, for the high pressure data, which are the most relevant to mantle melting, Eq. 10 gives a very good fit to the data. This is illustrated by the good correlation ($R = 0.84$) between the observed and predicted values of D_{Th} for the high pressure data (excluding those of Beattie [7]).
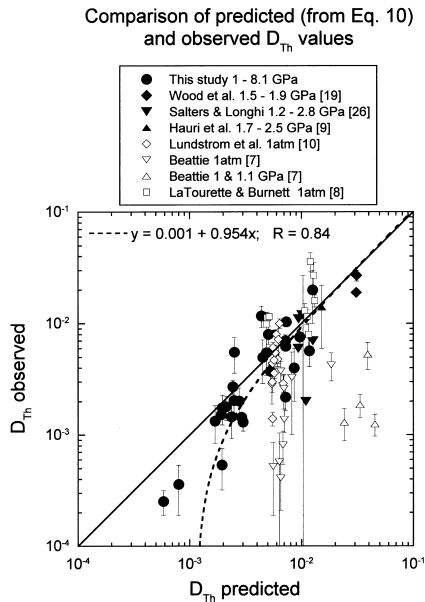
Comparison of predicted (from Eq. 10) and observed D_{Th} values

Legend:
- ● This study 1 - 8.1 GPa
- ◆ Wood et al. 1.5 - 1.9 GPa [19]
- ▼ Salters & Longhi 1.2 - 2.8 GPa [26]
- ▲ Hauri et al. 1.7 - 2.5 GPa [9]
- ◇ Lundstrom et al. 1atm [10]
- ▽ Beattie 1atm [7]
- △ Beattie 1 & 1.1 GPa [7]
- □ LaTourette & Burnett 1atm [8]

$y = 0.001 + 0.954x; \quad R = 0.84$

Fig. 5. Comparison of observed D_{Th} values (this study and literature data) with D_{Th} values predicted from temperature, pressure and crystal composition using Eq. 10. Linear regression of all high pressure data (broken line; excluding the data of Beattie [7]) gives $D_{Th}^{observed} = 0.0011 + 0.954 D_{Th}^{predicted}$ and a correlation coefficient of $r = 0.84$. Error bars (shown if bigger than symbols) are ± 1 S.D. No error bars are plotted for data of Salters and Longhi (see text for discussion).

For garnet (experiments W&P 2311-07 and 2701-07) we obtained D_U/D_{Th} values of 4.9 and 3.3 at absolute D_U values of 0.020 and 0.024, respectively. These values are in excellent agreement with values from the literature [11,12]. For pigeonite (experiment W&P 122-1) we obtain D_U/D_{Th} of 2.8 and a D_U of 5×10^{-4}. These values are close to those reported for pyroxenes with similar low Ca content (i.e. Ca < 0.15 atoms per formula unit [19,26]).

6. Application to mantle melting

Key results of our study are that D_U/D_{Th} in clinopyroxene at the solidus of spinel lherzolite crosses over from values < 1.0 below 1.2 GPa to values > 1.0 above 1.2 GPa, and that absolute values of D_{Th} decrease by half along the spinel lherzolite solidus from 2×10^{-2} at 1 GPa to 1×10^{-2} at 3 GPa. This is illustrated in Fig. 6

where D_U/D_{Th} and D_{Th} values, calculated using Eqs. 2–4, 8 and 10, for compositions of near-solidus clinopyroxenes [14,15] are plotted as a function of pressure. These findings have important implications for the generation of ^{230}Th excess during mantle melting. The most important is that ^{230}Th excess may potentially be generated during melting of spinel lherzolite without the presence of garnet on the mantle solidus. Although a detailed survey of the importance of our new partitioning data for mantle melting is beyond the scope of this paper (and will be presented elsewhere), we will briefly discuss the implications with respect to the generation of ^{230}Th excess beneath mid-ocean ridges.

Young MORBs exhibit (^{230}Th/^{238}U) ratios ranging from ∼0.9 (i.e. ^{238}U excess) up to 1.35 (i.e. ^{230}Th excess) [42]. Most values are clustered in the range of 1.05–1.25, i.e. ^{230}Th excess is most commonly observed. Moreover, the observed ^{230}Th excess is inversely correlated with ridge axis depth [42], such that melting that initiates at great depth (shallow ridges) produces melts with a greater ^{230}Th excess, than melting that initiates at shallow depth (deep ridges). These observations have been previously explained by the presence of solidus garnet at the onset of melting beneath shallow mid-ocean ridges, i.e. a significant proportion of melt in these settings is derived
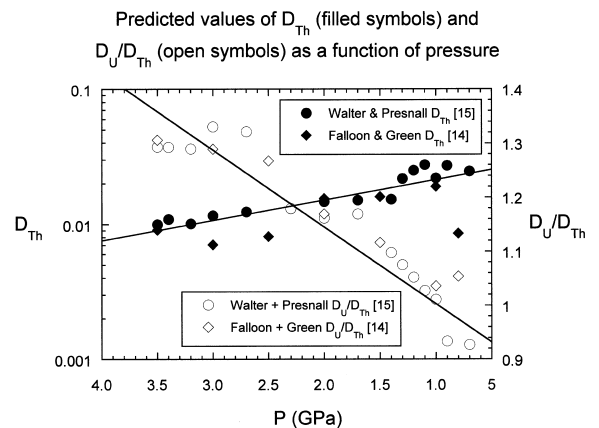

Predicted values of D_{Th} (filled symbols) and D_U/D_{Th} (open symbols) as a function of pressure

Legend:
- ● Walter & Presnall D_{Th} [15]
- ◆ Falloon & Green D_{Th} [14]
- ○ Walter + Presnall D_U/D_{Th} [15]
- ◇ Falloon + Green D_U/D_{Th} [14]

Fig. 6. Predicted D_{Th} and D_U/D_{Th} values (from Eqs. 2–4 and 10) for experimentally produced clinopyroxenes stable on the mantle solidus [14,15] as a function of pressure. Note that lines are included to depict the overall trend and are not obtained by linear regression.

from a deep mantle source [4]. An alternative possibility is that garnet-bearing lithologies, such as pyroxenite, are present within the spinel lherzolite field [44]. In both cases the ^{230}Th excess observed is a mixture of a garnet signal (large excess) and a clinopyroxene signal (negligible excess). Our results suggest an alternative explanation.

We performed dynamic melting calculations using the model of MeKenzie [1] in order to quantitatively estimate the amounts of ^{230}Th excess produced during mantle melting using our new partitioning data. Applying the D_U and D_{Th} partition coefficients calculated for near-solidus mantle clinopyroxenes (see above) and D_U and D_{Th} partition coefficients for olivine and orthopyroxene from the literature [12,19] we calculated bulk partition coefficients for U and Th as a function of depth along the mantle solidus (Table 4). U and Th partition coefficients for spinel were assumed insignificant [8]. The following mineral modes were used: 62% olivine, 20% orthopyrox-

ene, 17% clinopyroxene and 1% spinel (spinel lherzolite); and 60% olivine, 20% orthopyroxene, 10% clinopyroxene and 10% garnet (garnet lherzolite). Densities of the solid and the liquid were 3370 kg m^{-3} and 2700 kg m^{-3}, respectively. The porosity was set to 10^{-5}, melt production rate to 10^{-5} kg m^{-3} yr^{-1}, and upwelling velocity to 0.03 m yr^{-1}. These values correspond to a melt productivity rate of 0.01% km^{-1} for near-solidus melting, comparable to the values estimated by Hirschmann et al. [43] based on MELTS calculations. The value of 10^{-5} for porosity is a minimal value, consistent with that estimated by McKenzie [6].

The obtained values of ^{230}Th excess (Th*) are listed in Table 4 and plotted as a function of depth in Fig. 7. As can be seen ^{230}Th excesses from 1.08 of up to 1.34 can be generated within the spinel lherzolite stability field by using our new partitioning data. Moreover, the strong correlation between ^{230}Th excess and depth of the

Table 4
Parameters used for dynamic melting calculations and calculated Th excess (Th*)

Source[a]	Run	P (GPa)	Depth (km)[b]	T (°C)	D_{Th-Cpx}	D_U/D_{Th}	D_{U-Bulk}	$D_{Th-Bulk}$	Th*[c]
W&P	701-12	0.7	21.2	1225	0.0247	0.93	0.00424	0.00436	0.97
W&P	901-12	0.9	27.2	1240	0.0272	0.93	0.00467	0.00479	0.98
W&P	1002-10	1	30.2	1280	0.0220	1.01	0.00413	0.00390	1.05
W&P	1101-12	1.1	33.3	1255	0.0276	1.03	0.00516	0.00485	1.06
W&P	1203-10	1.2	36.3	1295	0.0250	1.05	0.00483	0.00442	1.09
W&P	1302-10	1.3	39.3	1310	0.0217	1.08	0.00433	0.00386	1.11
W&P	1406-04	1.4	42.3	1355	0.0153	1.10	0.00321	0.00277	1.14
W&P	66-17-5	1.7	51.4	1380	0.0151	1.17	0.00335	0.00273	1.20
W&P	2008-03	2	60.5	1424	0.0147	1.16	0.00326	0.00267	1.20
W&P	2303-04	2.3	69.6	1480	0.0131	1.18	0.00297	0.00239	1.21
W&P	2702-03	2.7	81.7	1507	0.0124	1.32	0.00314	0.00228	1.33
W&P	3002-03	3	90.7	1531	0.0117	1.33	0.00299	0.00215	1.34
W&P	3202-11	3.2	96.8[d]	1580	0.0101	1.29	0.00639	0.00228	2.58[d]
W&P	3403-11	3.4	102.8[d]	1580	0.0109	1.29	0.00650	0.00236	2.54[d]
W&P	3503-11	3.5	105.9[d]	1594	0.0100	1.29	0.00637	0.00227	2.58[d]
F&G	T-1516	0.8	24.2	1350	0.0086	1.05	0.00188	0.00162	1.14
F&G	T-1511	1	30.2	1285	0.0190	1.04	0.00370	0.00340	1.08
F&G	T-1989	1.5	45.4	1360	0.0160	1.12	0.00339	0.00289	1.16
F&G	T-1515	2	60.5	1420	0.0155	1.17	0.00344	0.00281	1.20
F&G	T-2086	2.5	75.6	1550	0.0081	1.27	0.00211	0.00155	1.30
F&G	T-2065	3	90.7	1600	0.0071	1.29	0.00190	0.00137	1.31
F&G	T-2087	3.5	105.9[d]	1600	0.0091	1.31	0.00614	0.00217	2.59[d]

[a] W&P = Walter and Presnall [15]; F&G = Falloon and Green [14].
[b] Calculated using an average density of 3370 kg m^{-3}.
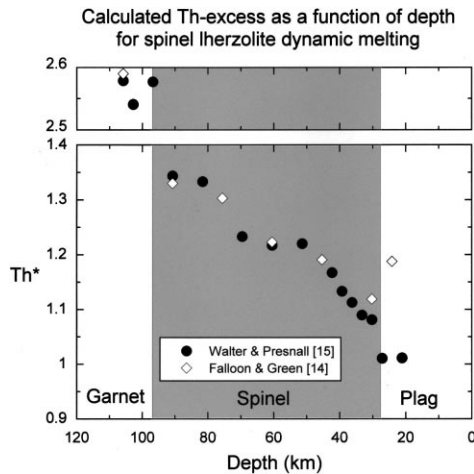[c] Th excess is expressed as the activity ratio (^{230}Th/^{238}U).
[d] Garnet present.

Fig. 7. Th excess (Th*) generated by dynamic melting of lherzolite as a function of depth. Boundaries between plagioclase-, spinel- and garnet lherzolite stability fields are depicted as vertical lines. Note the difference in scale for Th excess generated by melting of garnet lherzolite.

onset of melting is reminiscent of the inverse correlation between ^{230}Th excess and ridge axis depth found by Bourdon et al. [42] in their study of U-series disequilibria in a global MORB dataset. Furthermore, the maximum value of ^{230}Th excess obtained in that study, 1.348 from an Atlantic MORB, is in good agreement with the maximum value obtained in our models for melting just above the garnet–spinel boundary at 90 km depth (Th* = 1.31–1.34; Table 4). Thus for melting exclusively in the spinel lherzolite field our model can potentially account for both the absolute magnitude of MORB ^{230}Th excesses and the observed linear relationship between the extent of ^{230}Th excess and the apparent depth of beginning of melting beneath ocean ridges.

Our findings are at odds with many other studies of U-series disequilibria, which ascribe ^{230}Th excesses to the presence of garnet in the source region. Such conclusions are in large part a consequence of the available partitioning data which suggested that clinopyroxene was incapable of producing the ^{230}Th excesses observed. Our new partitioning data delineate more clearly what excesses can (and cannot) be generated by melting of spinel lherzolite. Appreciably greater excesses

can, of course, still be generated in the presence of garnet (Fig. 7). However, it is as yet unclear whether garnet is *required* to observe the U-series data. We recognise that other geochemical (e.g. Lu–Hf isotopes [48]) and geophysical (e.g. seismic tomography [49]) lines of evidence might be suggestive of garnet in the source regions of MORB. It is not our intention to dismiss such evidence, nor to eliminate garnet as a contributor to the observed ^{230}Th excesses in MORB and other mantle-derived melts. We simply emphasise that clinopyroxene has a much more important role in generating ^{230}Th excesses than has been previously recognised. The ability of spinel lherzolite melting to generate a linear relationship between the depth to the onset of melting and the magnitude of ^{230}Th excess appears to be a particularly attractive feature of our model. Such linearity is less readily explained by mixing-in of partial melts of garnet-bearing heterogeneities in the mantle, unless these are systematically distributed with depth, or unless the extent of melting is determined largely by the abundance of heterogeneities rather than the depth at which melting is initiated.

Such is the potential capacity of clinopyroxene for generating ^{230}Th excesses, that it is worth exploring those conditions under which ^{230}Th excesses will not be observed through melting of garnet-free lherzolites. Mantle porosity has an important influence on the extent of ^{230}Th excess that can be generated (e.g. [7,19]). If the porosity is significantly larger than the bulk D for U then no ^{230}Th excess can be generated [1]. However, as bulk D_U for garnet lherzolite is only two to four times higher than for spinel lherzolite (Table 4), the same constraint applies equally to both lithologies. In fact the observed ^{226}Ra excesses in MORB [46] require that porosity must be significantly less than the bulk partition coefficient for Th during melting, i.e. $< 10^{-3}$. Such a high value will reduce the ^{230}Th excesses that can be generated in spinel lherzolite, but only by a few percent. For example, the maximum ^{230}Th excess that can be generated in spinel lherzolite (Table 4) is reduced from 1.34 (at a porosity of 10^{-5}) to 1.26 (at 10^{-3}). We conclude that a better constraint on mantle porosity would be useful, but is unlikely to compromise our findings.

The melt production rate also has an important influence on ^{230}Th excesses (e.g. [7,19]). The value that we have chosen (10^{-5} kg m^{-3} yr^{-1}) is at the low end of generally accepted values. The corresponding melt productivity (0.01% km^{-1}) is appreciably lower than the average melt productivity over the entire melting column, which is constrained to produce the observed crustal thickness (i.e. 0.1–0.2% km^{-1}). However, a low value is consistent with theoretical [43] and experimental [45] evidence that melt productivity is very low close to the near-solidus region where all ^{230}Th excesses are generated. Increasing the melt productivity to 0.025% km^{-1} (the value estimated by Hirschmann et al. [43]), at a constant upwelling rate of 0.03 m yr^{-1}, will reduce the maximum ^{230}Th excess that can be generated from 1.34 to 1.28. Combining a higher melt productivity (0.025% km^{-1}) with a higher porosity (10^{-3}) still only reduces the maximum ^{230}Th excess to 1.22. Again, we conclude that better constraints on melt productivity (and upwelling rate) would be of great value, but are unlikely to significantly compromise our findings.

Finally, the composition of solidus clinopyroxenes is also important in controlling the extent of U–Th fractionation, and hence the magnitude of ^{230}Th excess. The compositional data that we have used are the most reliable available, but we recognise that if the true mantle clinopyroxenes are significantly more calcic (and hence have large r_0^{M2}) than those used here, then smaller ^{230}Th excesses will result. Similarly, if bulk compositional variations in the spinel lherzolite source lead to changes in r_0^{M2} then changes in ^{230}Th excess will result. In this context it is interesting to note that Asmeron et al. [28] use the combined ^{231}Pa and ^{230}Th excesses in lithospheric melts from the western USA to constrain the D_U/D_{Th} ratio in the source region of three samples to be 0.98 ± 0.02, 1.01 ± 0.04 and 1.06 ± 0.11 (weighted mean = 1.00 ± 0.01). This is a robust and incisive constraint, which unfortunately the authors use to conclude that the proposal of Wood et al. [19] regarding clinopyroxene–melt U–Th partitioning is unfounded. On the contrary, the observation that D_U/D_{Th} is within a few % of unity simply indicates that r_0^{M2} at the onset of melting beneath the western USA is approximately 1.00 ± 0.05 Å (Fig. 4). If the clinopyroxenes in the lithospheric source region are similar in composition to those adopted here, then this range in r_0^{M2} is suggestive of initiation of melting at pressures of 0.8–1.3 GPa. The three asthenospheric melts from the same region [28] have calculated source region D_U/D_{Th} values of 1.54 ± 0.19, 1.79 ± 0.05 and 1.87 ± 0.05. We concur with the authors that such large values are unlikely to have been produced by melting of spinel lherzolite (see Fig. 7), and that garnet lherzolite is a more plausible source.

7. Conclusions

Experimental determination of U and Th partitioning between clinopyroxene and silicate melts in a wide range of synthetic systems demonstrates that sub-calcic aluminous clinopyroxenes, of the variety typical for the mantle solidus, preferentially incorporate U relative to ^{230}Th. Consequently melting of a sub-calcic aluminous clinopyroxene-bearing source rock can generate excesses of ^{230}Th, even in the absence of garnet, a finding at odds with previous studies, which were constrained to using partitioning data for inappropriately calcic clinopyroxenes. Simple, one-dimensional dynamic models of mantle melting show that the extent of ^{230}Th excess that can be generated by spinel lherzolite melting is consistent with the observed range for MORB. Moreover, the ^{230}Th excess generated correlates linearly with the depth at which melting begins, in a fashion that resembles the correlation between ^{230}Th excess and ridge axial depth for a global MORB dataset. Plausible variations in melting parameters, especially porosity and melt productivity, reduce only slightly the maximum ^{230}Th excess that can be generated by melting of spinel lherzolite. Although our results by no means eliminate a role for garnet in the generation of MORB, they confirm theoretical predictions that clinopyroxene plays an important role in generating ^{230}Th excesses during mantle melting. This role cannot be ignored when modelling U-series disequilibrium during mantle melting.

Acknowledgements

References

[1] D. McKenzie, ^{230}Th–^{238}U disequilibrium and the melting process beneath ridge axes, Earth Planet. Sci. Lett. 72 (1985) 149–157.

[2] M. Condomines, Ch. Hémond, C.J. Allègre, U–Th–Ra radioactive disequilibria and magmatic processes, Earth Planet. Sci. Lett. 90 (1988) 243–262.

[3] J.B. Gill, M. Condomines, Short lived radioactivity and magma genesis, Science 257 (1992) 1368–1376.

[4] T.Z. LaTourette, A.K. Kennedy, G.J. Wasserburg, Uranium–thorium fractionation by garnet – evidence for a deep source and rapid rise of oceanic basalts, Science 261 (1993) 739–742.

[5] T. Elliott, Fractionation of U and Th during mantle melting: A reprise, Chem. Geol. 139 (1997) 165–183.

[6] D. McKenzie, Some remarks on the movement of small melt fractions in the mantle, Earth Planet. Sci. Lett. 95 (1989) 53–72.

[7] P. Beattie, The generation of uranium series disequilibria by partial melting of spinel peridotite: Constraints from partitioning studies, Earth Planet. Sci. Lett. 117 (1993) 379–391.

[8] T.Z. LaTourette, D.S. Burnett, Experimental determination of U and Th partitioning between clinopyroxene and natural and synthetic basaltic liquid, Earth Planet. Sci. Lett. 110 (1992) 227–244.

[9] E.H. Hauri, T.P. Wagner, T.L. Grove, Experimental and natural partitioning of Th, U, Pb and other trace elements between garnet and clinopyroxene and basaltic liquids, Chem. Geol. 117 (1994) 149–166.

[10] C.C. Lundstrom, H.F. Shaw, F.J. Ryerson, D.L. Phinney, J.B. Gill, Q. Williams, Compositional controls on the partitioning of U, Th, Ba, Pb, Sr, and Zr between clinopyroxene and haplobasaltic melts: Implications for uranium series disequilibria in basalts, Earth Planet. Sci. Lett. 128 (1994) 407–423.

[11] P. Beattie, Uranium–thorium disequilibria and partitioning on melting of garnet peridotite, Nature 363 (1993) 63–65.

[12] W. Van Westrenen, J.D. Blundy, B.J. Wood, Crystal-chemical controls on trace element partitioning between garnet and anhydrous silicate melt, Am. Mineral. 84 (1999) 838–847.

[13] E. Takahashi, I. Kushiro, Melting of a dry peridotite at high pressures and temperatures and basalt magma genesis, Am. Mineral. 68 (1983) 859–879.

[14] T.J. Falloon, D.H. Green, Anhydrous partial melting of MORB pyrolite and other peridotite compositions at 10 kbar. Implications for the origin of primitive MORB glasses, Mineral. Petrol. 37 (1987) 181–219.

[15] M.J. Walter, D.C. Presnall, Melting behaviour of simplified lherzolite in the system CaO–MgO–Al$_2$O$_3$–SiO$_2$–Na$_2$O from 7 to 35 kbar, J. Petrol. 35 (1994) 329–359.

[16] G.H. Gudfinnsson, D.C. Presnall, Melting relations of model lherzolite in the system CaO–MgO–Al$_2$O$_3$–SiO$_2$ at 2.4–3.4 GPa and the generation of komatiites, J. Geophys. Res. 101 (1996) B701–B709.

[17] K. Hirose, I. Kushiro, The effect of melt segregation on polybaric mantle melting: Estimation from incremental melting experiments, Phys. Earth Planet. Int. 107 (1998) 111–118.

[18] G.H. Gudfinnsson, D.C. Presnall, Melting behaviour of model lherzolite in the system CaO–MgO–Al$_2$O$_3$–SiO$_2$–FeO at 0.7–2.8 GPa, J. Petrol. 41 (2000) 1241–1269.

[19] B.J. Wood, J.D. Blundy, J.A.C. Robinson, The role of clinopyroxene in generating U-series disequilibrium during mantle melting, Geochim. Cosmochim. Acta 63 (1999) 1613–1620.

[20] M.B. Baker, E.M. Stolper, Determining the composition of high-pressure melts using diamond aggregates, Geochim. Cosmochim. Acta 58 (1994) 2811–2827.

[21] J.D. Blundy, B.J. Wood, Prediction of crystal–melt partition coefficients from elastic moduli, Nature 372 (1994) 452–454.

[22] N. Onuma, H. Higuchi, H. Wakita, H. Nagasawa, Trace element partitioning between two pyroxenes and the host lava, Earth Planet. Sci. Lett. 5 (1968) 47–51.

[23] B.J. Wood, J.D. Blundy, A predictive model for rare earth element partitioning between clinopyroxene and anhy-

drous silicate melt, Contrib. Mineral. Petrol. 129 (1997) 166–181.

[24] J.A.C. Robinson, B.J. Wood, J.D. Blundy, The beginning of melting of fertile and depleted peridotite at 1.5 GPa, Earth Planet. Sci. Lett. 155 (1998) 97–111.

[25] R.D. Shannon, Revised effective ionic radii in oxides and fluorides, Acta Crystallogr. A32 (1976) 751–757.

[26] V.J.M. Salters, J. Longhi, Trace element partitioning during the initial stages of melting beneath mid-ocean ridges, Earth Planet. Sci. Lett. 166 (1999) 15–30.

[27] T. Benjamin, W.R. Heuser, D.S. Burnett, M.G. Seitz, Actinide crystal–liquid partitioning for clinopyroxene and $Ca_3(PO_4)_2$, Geochim. Cosmochim. Acta 44 (1980) 1251–1264.

[28] Y. Asmerom, H. Cheng, R. Thomas, M. Hirschmann, R.E. Edwards, Melting of the Earth's lithospheric mantle inferred from protactinium–thorium–uranium isotopic data, Nature 406 (2000) 293–296.

[29] J.D. Blundy, T.J. Falloon, B.J. Wood, J.A. Dalton, Sodium partitioning between clinopyroxene and silicate melts, J. Geophys. Res. 100 (1995) 15501–15516.

[30] E.M. Chamorro-Perez, J.A. Wartho, R. Brooker, B.J. Wood, S. Kelley, J.D. Blundy, Ar partitioning between clinopyroxene and silicate melt to high pressure, Geochim. Cosmochim. Acta (submitted).

[31] M. Schosnig, E. Hoffer, Compositional dependence of REE partitioning between diopside and melt at 1 atmosphere, Contrib. Mineral. Petrol. 133 (1998) 205–216.

[32] M.S. Ghiorso, R.O. Sack, Chemical mass transfer in magmatic process IV. A revised and internally consistent thermodynamic model for the interpretation and extrapolation of liquid–solid equilibria in magmatic systems at elevated temperatures and pressures, Contrib. Mineral. Petrol. 119 (1995) 197–212.

[33] W. Van Westrenen, J.D. Blundy, B.J. Wood, Effect of Fe^{2+} on garnet–melt trace element partitioning: Experiments in FCMAS and quantification of crystal-chemical controls in natural systems, Lithos 53 (2000) 191–203.

[34] D.J. Frost, B.J. Wood, Experimental measurements of the graphite–C–O equilibrium and CO_2 fugacities at high temperature and pressure, Contrib. Mineral. Petrol. 121 (1995) 303–308.

[35] J.A.C. Robinson, B.J. Wood, The depth of the spinel to garnet transition at the peridotite solidus, Earth Planet. Sci. Lett. 164 (1998) 277–284.

[36] D. Walker, M.A. Carpenter, C.M. Hitch, Some simplifi-

cations to multianvil devices for high pressure experiments, Am. Mineral. 75 (1990) 1020–1028.

[37] H. Nagasawa, Trace element partition coefficient in ionic crystals, Science 152 (1966) 767–769.

[38] J.C. Brice, Some thermodynamic aspects of the growth of strained crystals, J. Cryst. Growth 28 (1975) 249–253.

[39] B.J Wood, J.D. Blundy, The effect of cation charge on crystal–melt partitioning of trace elements, Earth Planet. Sci. Lett. 188 (2001) 59–71.

[40] P. Richet, Y. Bottinga, Thermochemical properties of silicate liquids and glasses: a review, Rev. Geophys. 24 (1986) 1–25.

[41] B.J. Wood, Thermodynamics of multicomponent systems containing several solid solutions, Rev. Mineral. 17 (1987) 71–96.

[42] B. Bourdon, A. Zindler, T. Elliott, C.H. Langmuir, Constraints on mantle melting at mid-ocean ridges from global ^{238}U–^{230}Th disequilibrium data, Nature 384 (1996) 231–235.

[43] M.M. Hirschmann, P.D. Asimow, M.S. Ghiorso, E.M. Stolper, Calculation of peridotite partial melting from thermodynamic models of minerals and melts. III. Controls on isobaric melt production and the effect of water on melt production, J. Petrol. 40 (1999) 831–851.

[44] M.M. Hirschmann, E.M. Stolper, A possible role for garnet pyroxenite in the origin of the 'garnet signature' in MORB, Contrib. Mineral. Petrol. 124 (1996) 185–208.

[45] J. Pickering-Witter, A.D. Johnston, The effects of variable mineral proportions on the melting systematics of fertile peridotitic assemblages, Contrib. Mineral. Petrol. 140 (2000) 190–211.

[46] K.H. Rubin, J.D. Macdougall, Dating of neovolcanic MORB using (^{226}Ra/^{230}Th) disequilibrium, Earth Planet. Sci. Lett. 101 (1990) 313–322.

[47] B.O. Mysen, D. Virgo, F.A. Seifert, The structure of silicate melts: Implications for chemical and physical properties of natural magma, Rev. Geophys. Space Phys. 20 (1982) 353–383.

[48] V.J.M. Salters, The generation of mid-ocean ridge basalts from the Hf and Nd perspective, Earth Planet. Sci. Lett. 141 (1996) 109–123.

[49] D.R. Toomey, W.S. Wilcock, S.C. Solomon, W.C. Hammond, J.A. Orcutt, Mantle seismic structure beneath the MELT region of the East Pacific Rise from P and S wave tomography, Science 280 (1998) 1224–1227.